Linking the Population of Binary Black Holes with the Stochastic Gravitational-Wave Background

Olivia X. Laske,[1] Mentors: Patrick M. Meyers,[2] and Arianna Renzini[2]

[1]*Department of Physics and Astronomy, Macalester College, 1600 Grand Av, Saint Paul, MN 55105, USA*
[2]*Division of Physics, California Institute of Technology, 1200 E. California Blvd, Pasadena, CA 91125, USA*

(Dated: 22 September 2023)

ABSTRACT

The astrophysical stochastic gravitational-wave background (SGWB) is the product of overlapping waveforms that create a single unresolvable background. While current LIGO sensitivity is insufficient to uncover the SGWB, future space-based detectors and Third Generation (3G) experiments are expected to probe deep enough for detection. In addition, predictions of the SGWB can still constrain future searches as well as provide insight into star formation, merger history, and mass distribution. Here, two primary methods are used to calculate a theoretical SGWB. The first method integrates over a precomputed mass distribution probability grid, while the second employs Monte Carlo integration with simulated data. After standardizing a prior dictionary across both methods, the output energy density spectra is analyzed with regard to parameters such as binary black hole mass and merger rate. Increasing the maximum merger mass shifts the gravitational-wave (GW) energy density peak to lower frequencies, while increasing merger rate parameters increases the GW energy density.

1. INTRODUCTION

Gravitational-waves (GWs) are perturbations in space-time produced by large scale, highly energetic events. GWs were first observed in 2015 by the Laser Interferometer Gravitational-Wave Observatory (LIGO), located in Livingston, Louisiana and Hanford, Washington, with the detection of GW150914, a binary black hole merger.[1] LIGO is joined by several other ground-based GW observatories, including Virgo in Italy, GEO600 in Germany, and KAGRA (Kamioka Gravitational-Wave Detector) in Japan. In addition, the space-based detector Laser Interferometer Space Antenna (LISA) and Third Generation (3G) experiments Einstein Telescope (ET) and Cosmic Explorer (CE) are expected to launch in the 2030s.

LIGO takes the form of a Michelson interferometer, in which an incident laser beam is split into orthogonal reflected and transmitted beam components along the

olaske@macalester.edu

pmeyers@caltech.edu

arenzini@caltech.edu

two arms of the detector. The beams are subsequently reflected back toward the beam splitter and recombined. During a GW event, the arms of the detector are compressed and rarefied, causing the two beams to shift out of phase and form a detectable interference pattern.

LIGO relies on cross correlation to confirm GW signals. The numerous noise sources, ranging from the seismic noise of ocean waves and earthquakes to the thermal noise of suspension mirror resonance frequencies, prove difficult to distinguish from GW signals, especially as the strain produced by GWs is on the order of 10^{-21} m.[1] Ensuring signal presence at multiple interferometers both reliably confirms GW signals and allows for more accurate sky localization.

GW signals are often categorized into continuous, compact binary inspiral, burst, and stochastic types. Continuous GWs are produced by large, rotating systems, such as neutron stars, and appear as a sinusoidal pattern of detector strain over long periods of time.[2] Compact binary inspirals arise from mergers of dense objects, such as black holes and neutron stars, and are characterized by a chirp signal in time-frequency space.[3] Through O3, LIGO has detected 90 GW events stemming from

compact binary inspirals.[2] Burst GW sources include Type II supernovae and are measured on short time scales.[4] Finally, stochastic signals are the sum of numerous unresolved GW sources that form a background. LIGO has yet to detect continuous, burst, and stochastic signals.

2. THE STOCHASTIC GRAVITATIONAL WAVE BACKGROUND

The stochastic gravitational-wave background (SGWB) is of particular interest, especially as the involved GWs can originate from the very early Universe, not long after the Big Bang. Because the Universe at the time was opaque to photons, the SGWB is one of the only means of studying this era. In addition, understanding the effect of the binary black hole (BBH) population on the SGWB constrains properties such as merger rate and mass distribution.

The SGWB is often divided into two categories: cosmological and astrophysical. Cosmological sources include events that occurred in the early Universe, such as inflation, during which rapid expansion drove GWs into an isotropic background. Astrophysical sources are comprised of individual events such as mergers and pulsars. Figure 1 depicts the predicted SGWBs for several cosmological and astrophysical sources across the frequency spectrum.
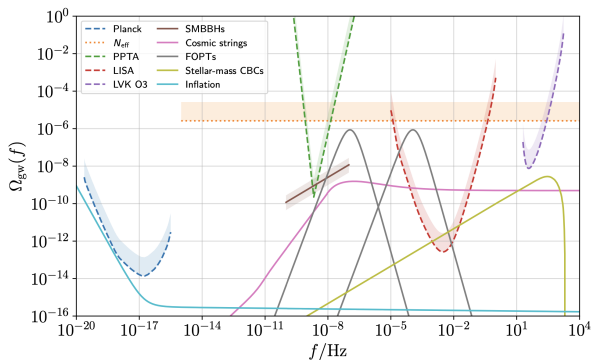

Figure 1. Predicted GW backgrounds from different sources across the frequency spectrum. Figure from (5).

Each color represents a different source of GWs. For instance, the pink curve originates from cosmic strings, and the blue curve is due to inflation. The frequency sensitivity of LIGO ranges from 10 Hz to 10 kHz,[6] which encapsulates the predicted SGWB arising from stellar-mass compact binary coalescences (CBCs). The SGWB from supermassive binary black holes (SMBBHs) lies outside of this range from 10^{-10} Hz to 10^{-7} Hz. The

project specifically focuses on stellar-mass BBHs (1 to 100 $M_\odot$), which are expected to be the majority of the BBH signal in the LIGO frequency range.

The dashed lines represent the sensitivity curves for different detectors. For instance, the dashed green curve corresponds to the Parkes Pulsar Timing Array (PPTA). The curve intersects the predicted background for SMBBHs, which is consistent with recent evidence for a SGWB at nanohertz frequencies.[7] The dashed red curve, on the other hand, is for the Laser Interferometer Space Antenna (LISA). The overlap with the yellow curve predicts that LISA will uncover the SGWB originating from stellar-mass CBCs, first-order phase transitions (FOPTs), and cosmic strings.

Detector sensitivity and resolution limits result in unresolved GW signals, which overlap to create a measurable SGWB. With current detector sensitivity in the LIGO frequency band, though, the SGWB is undetectable, as illustrated in Figure 2.
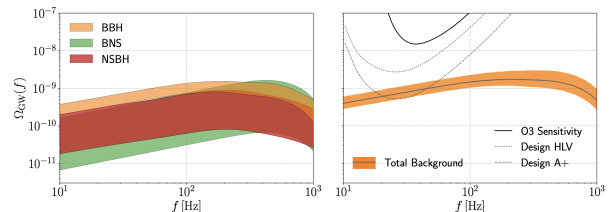
Figure 2. Current detector limits with regard to the SGWB. Figure from (5).

The orange bounds predict the combined SGWB from BBHs, BNSs, and NSBHs. The solid black, dashed, and dot-dashed curves are the sensitivity curves for the O3, Design HLV, and Design A+ observing runs, respectively. While the O3 and Design HLV curves do not intersect the total background bounds, Design A+ LIGO, as well as detectors LISA, ET, and CE, will begin to probe the sensitivities required to detect the SGWB from unresolved compact binary mergers.

Detectors must be sufficiently far apart in order to ensure that they are not receiving identical noise sources. However, one consequence of physically distant detectors is the overlap reduction function $\Gamma(f)$, shown for the LVK network in Figure 3. A value of $|\Gamma(f)| = 1$ occurs when the measured power is equal to the GW power after cross-correlating data. A value of $|\Gamma(f)| < 1$, however, occurs when the measured power is less than the GW power, signifying reduced sensitivity.
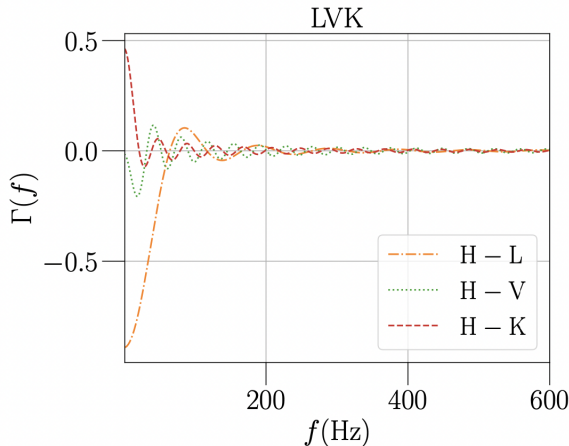
Figure 3. Overlap reduction function for the LVK network. Figure from (5).

An oscillating GW signal is time-shifted between the detectors, which reduces signal correlation between them. A consequence of time-shifted signals is that the magnitude of the overlap reduction function is greatest at lower frequencies, then rapidly dampens with increasing frequency.

For detectors that are further apart, such as LIGO Hanford and Virgo, $|\Gamma(f)|$ is decays more quickly. In addition, $|\Gamma(0)|$ decreases as detector separation increases. As a result, assuming a uniform, isotropic, unpolarized, and Gaussian SGWB, LIGO is more sensitive to low-frequencies, where the wavelength is significantly greater than the distance between the detectors.

Furthermore, the detectors are not optimally oriented, which causes $|\Gamma(f)|$ to decrease. Detectors that are either parallel or antiparallel maximize signal correlation by ensuring that strain amplitude is identical between the sites.

3. METHODS

Several different methods may be used to calculate the SGWB. The first method, developed by Thomas Callister (hereby referred to as the Gridded Method), uses a predefined mass distribution to create a grid of (m_1, q) points, converts them to $(\ln M_{\text{tot}}, q)$ space with the Jacobian, and calculates the spectral energy density at each grid point. The second method, devloped in C by Tania Regimbau and rewritten in Python by Arianna Renzini (the Monte Carlo Method), generates a frequency domain waveform and calculates the power spectral density for each injection in a list of injections. The third method (Combined Method) combines the previous two methods and uses a list of injections to define a mass distribution.

3.1. Theoretical Calculation of the SGWB

The SGWB is typically modeled by a power law of the following form:

$$\Omega_{\text{GW}}(f) = \Omega_{GW}(f_{\text{ref}}) \left(\frac{f}{f_{\text{ref}}}\right)^{\alpha}, \quad (1)$$

where $\Omega_{\text{GW}}(f)$ is dimensionless GW energy density, f is frequency, and α is the spectral index of the signal. According to literature, α is expected to be $2/3$.[5], [8] The GW energy density can be decomposed as follows:

$$\Omega_{\text{GW}}(f) = \frac{1}{\rho_c} \int_0^\infty dz \frac{N(z)}{1+z} \left[f_r \frac{dE_{\text{GW}}}{df_r}\right]_{f_r = f(1+z)}, \quad (2)$$

$$\rho_c = \frac{3H_0^2}{8\pi G}, \quad (3)$$

where ρ_c is critical density, $N(z)$ is number of GW sources as a function of redshift, z is redshift, dE_{GW}/df_r is spectral energy density, f_r is rest frame frequency, $H_0 = 67.4$ km s^{-1} Mpc^{-1} is the Hubble constant (see Appendix A), and $G = 6.6743015 \cdot 10^{-11}$ m^3 kg^{-1} s^{-2} is the universal gravitational constant. The integral of Equation 2 encompasses the entirety of redshift history. One interpretation of Equation 2 is that the components inside the integral multiply $N(z)$ by the spectral energy density weighted by f. At $z = 0$, $f_r = f$, and $\Omega_{\text{GW}}(f) = f(N_0/\rho_c)(dE_{\text{GW}}/df)$, demonstrating that Ω_{GW} is proportional to $N(z)$.

Fractional energy density can be averaged over source parameters θ. In addition, $N(z)$ can be rewritten in terms of event rate, redshift, and the Hubble parameter. Therefore, Equation 2 becomes the following after removing f from the integral:

$$\Omega_{\text{GW}}(f) = \frac{f}{\rho_c} \int_0^{z_{\text{max}}} dz \frac{\mathcal{R}(z)}{(1+z)H(z)} \left\langle \frac{dE_{\text{GW}}}{df_r}\bigg|_{f_r = f(1+z)} \right\rangle, \quad (4)$$

$$\left\langle \frac{dE_{\text{GW}}}{df_r} \right\rangle = \int d\theta p(\theta) \frac{dE_{\text{GW}}(\theta; f_r)}{df_r}, \quad (5)$$

where z_{max} is the maximum redshift for a BBH, $\mathcal{R}(z) = dN(z)/dt$ is the BBH merger rate, and $H(z)$ is the Hubble parameter as a function of redshift (see Appendix A).

3.2. Standard Prior Dictionary

In order to ensure that parameters remain consistent across all methods, a set of standard `bilby` priors is

defined as in Table 1. `mass_1` is the greater component mass, `mass_ratio` is defined as m_2/m_1, `chi_1` and `chi_2` are the component spins, `theta_jn` is the inclination angle of the merger, `geocent_time` is the elapsed geocentric time after the start of the observation period T_{obs} before the merger, and `redshift` is the redshift of the merger. Both `mass_1` and `mass_ratio` employ a power law distribution, while `theta_jn` and `geocent_time` use a uniform distribution. The project did not consider spin.

Prior	Distribution	Parameters
`mass_1`	Power Law	$\alpha = -2.3$
`mass_ratio`	Power Law	$\alpha = 1.5$
`chi_1`	0	0
`chi_2`	0	0
`theta_jn`	Uniform	$\min = 0$, $\max = 2\pi$
`geocent_time`	Uniform	$\min = 0$, $\max = T_{\mathrm{obs}}$
`redshift`	$\propto \frac{1}{1+z} \mathcal{R}(z) \frac{dV_c}{dz}$	$\min = 0$, $\max = 10$

Table 1. Prior distributions used in the Monte Carlo Method.

A separate `redshift` prior was defined using the merger rate and comoving volume per unit redshift. Redshift bins are set from $z = 0$ to $z = 10$ with $dz = 0.01$.

$$p(z) \propto \frac{1}{1+z} \mathcal{R}(z) \frac{dV_c}{dz}. \tag{6}$$

The merger rate $\mathcal{R}(z)$ is often modelled as follows:

$$\mathcal{R}(z) = \mathcal{C}(\alpha, \beta, z_{\mathrm{p}}) \frac{\mathcal{R}_0 (1+z)^\alpha}{1 + (\frac{1+z}{1+z_{\mathrm{p}}})^{\alpha+\beta}}, \tag{7}$$

$$\mathcal{C}(\alpha, \beta, z_{\mathrm{p}}) = 1 + (1+z_{\mathrm{p}})^{-(\alpha+\beta)}, \tag{8}$$

where $\mathcal{R}_0$ is the current merger rate and $\mathcal{C}(\alpha, \beta, z_{\mathrm{p}})$ is a normalization constant to satisfy the boundary condition $\mathcal{R}(0) = \mathcal{R}_0$. Values α and β shape the growth and decay of $\mathcal{R}(z)$ before and after peak redshift z_{p}.[9]

Figure 4 depicts the normalized redshift probability distribution for $\alpha = 3.2$, $\beta = 3.4$, $z_{\mathrm{p}} = 1.9$, and $\mathcal{R}_0 = 28.3$ Gpc^{-3} yr^{-1}. The peak in the graph represents cosmic noon, after which the rate of BBHs rapidly declines.

3.3. *Calculation of the SGWB with the Gridded Method*

The Gridded Method takes form in four distinct steps:
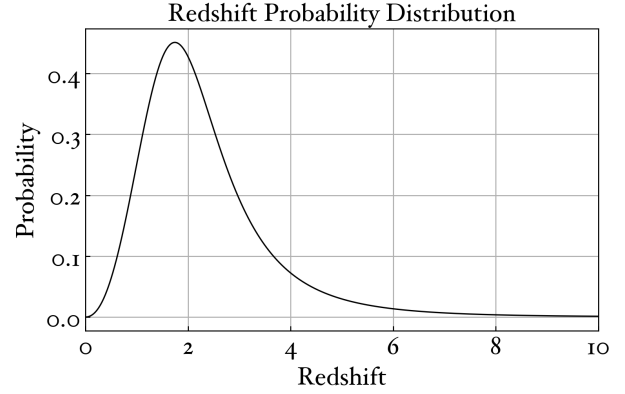
Figure 4. Redshift probability distribution using $\alpha = 3.2$, $\beta = 3.4$, $z_{\mathrm{p}} = 1.9$, and $\mathcal{R}_0 = 28.3$ Gpc^{-3} yr^{-1}.

1. Define the local merger rate.

2. Calculate the merger rate.

3. Determine the mass distribution probability grid.

4. Calculate the GW energy density Ω_{GW}.

The steps are described in the following sections.

3.3.1. *Definition of the Local Merger Rate*

The local merger rate describes the merger rate, which is the total number of mergers that occur per cubic Gpc per year, at $z = 0$. A BBH local merger rate is defined for subsequent merger rate density normalization such that $\mathcal{R}(z)_{\mathrm{norm}} = \mathcal{R}_0(\mathcal{R}(z)/\mathcal{R}(0))$. The Gridded Method uses $\mathcal{R}_0 = 28.3$ Gpc^{-3} yr^{-1}, the Power Law + Peak BBH merger rate ($z = 0.2$) from (10).

3.3.2. *Calculate of the Merger Rate*

The merger rate is calculated from Equations 7 and 8 for each redshift bin inputting $\alpha = 3.2$, $\beta = 3.4$, $z_{\mathrm{p}} = 1.9$, and $\mathcal{R}_0 = 28.3$ Gpc^{-3} yr^{-1}. Because the redshift prior uses an identical model and redshift bins, the array of merger rates directly maps to the array of redshift probabilities. Figure 5 displays a plot of the merger rate as a function of redshift.

3.3.3. *Determination of the Mass Distribution Probability Grid*

The minimum and maximum BH masses are set such that $m_{\min} = 5$ M$_\odot$ and $m_{\max} = 50$ M$_\odot$. A probability grid of the mass distribution is defined in (m_1, q) space using `prior.prob` on the standard `bilby` priors. The probabilities are then converted to $(\ln M_{\mathrm{tot}}, q)$ space with the Jacobian and normalized. (11) provides a table of Jacobians that converts between mass parameter pairs.

$$\frac{dP}{d\ln M_{\mathrm{tot}} dq} = \frac{dP}{dm_1 dq} \frac{M_{\mathrm{tot}}}{(1+q)}. \tag{9}$$
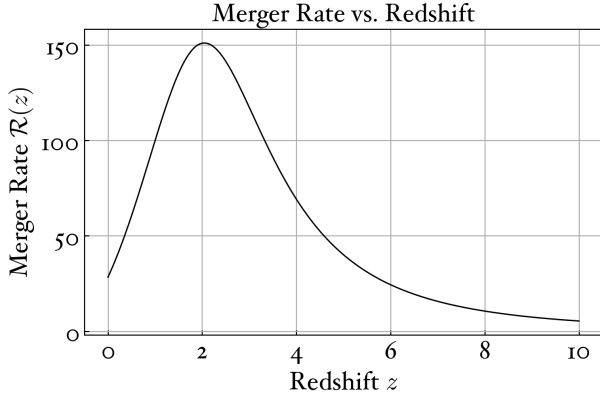
Figure 5. Merger rate using $\alpha = 3.2$, $\beta = 3.4$, $z_{\mathrm{p}} = 1.9$, and $\mathcal{R}_0 = 28.3$ Gpc^{-3} yr^{-1}.

While the mass distribution was defined in (m_1, q) space for the project, the priors may be defined in terms of other mass parameter pairs as well. For instance, if the standard priors were alternatively defined in (m_1, m_2) space, Equation 9 is revised to the following:

$$\frac{dP}{d\ln M_{\mathrm{tot}} dq} = \frac{dP}{dm_1 dm_2} \frac{M_{\mathrm{tot}}^2}{(1+q)^2}. \tag{10}$$

3.3.4. *Calculation of the GW Energy Density*

Once the mass distribution probability grid has been determined, the GW energy density can be calculated.

For inspiralling compact binary systems, the spectral energy density $dE_{\mathrm{GW}}/df_{\mathrm{r}}$ is found as follows:

$$\frac{dE_{\mathrm{GW}}}{df} = \frac{(G\pi)^{2/3} \mathcal{M}^{5/3}}{3} H(f), \tag{11}$$

$$\mathcal{M} = \frac{(m_1 m_2)^{3/5}}{(m_1 + m_2)^{1/5}}, \tag{12}$$

$$H(f) = \begin{cases} f^{-1/3} & (f < f_{\mathrm{merge}}) \\ \frac{f^{2/3}}{f_{\mathrm{merge}}} & (f_{\mathrm{merge}} \leq f < f_{\mathrm{ring}}) \\ \frac{1}{f_{\mathrm{merge}} f_{\mathrm{ring}}^{4/3}} \left(\frac{f}{1 + (\frac{f - f_{\mathrm{ring}}}{\sigma/2})^2} \right)^2 & (f_{\mathrm{ring}} \leq f < f_{\mathrm{cutoff}}) \\ 0 & (f \geq f_{\mathrm{cutoff}}) \end{cases} \tag{13}$$

Here, $\mathcal{M}$ is chirp mass, m_1 and m_2 are component masses, f is frequency, f_{merge} is the merger frequency, f_{ring} is the ringdown frequency, f_{cutoff} is the cutoff frequency, and σ is the width of the Lorentzian function around f_{ring}.[8] Parameters f_{merge}, f_{ring}, f_{cutoff}, and σ are given by Table I in (12).

$H(f)$ can be understood as the spectral shape of the GW energy density. Figure 6 depicts $H(f)$ for varying values of M_{tot} and z.
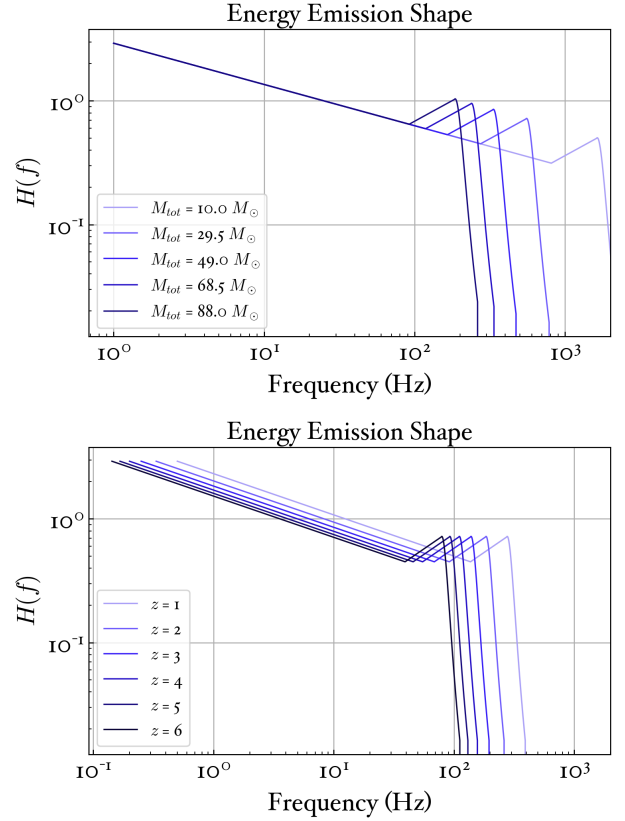
Figure 6. Spectral shape of GW energy density for varying values of M_{tot} and z.

The upper panel displays the shifting of $H(f)$ to lower frequencies and higher magnitudes as total mass increases, which confirms that more massive systems merge at lower frequencies with greater energy. The lower panel demonstrates that higher redshifts push $H(f)$ to lower frequencies and magnitudes, as expected. As redshift increases, signals both become fainter and decrease in frequency.

Probability $p(\theta)$ in Equation 5 is given for (m_1, q) by the mass distribution probability grid, and $\mathcal{M}$ can calculated from m_1 and $m_2 = m_1 q$. In other words, the average spectral energy density is calculated by integrating over each grid point. The merger rates and average spectral energy density are then inserted into Equation 4 to obtain the final GW energy density.

3.4. *Calculation of the SGWB with the Monte Carlo Method*

The Monte Carlo Method begins by sampling the priors given in Table 1. The resulting injections are inserted into the `Simulator` module of the Python library `pygwb` (Python-based library for gravitational-wave background-searches), which generates an IMR-PhenomPv2 waveform for each injection.[13] The module then calculates Ω_{GW} by summing the spectral energy density of each event:[14]

$$\frac{dE}{df} = |h_+|^2 + |h_\times|^2, \tag{14}$$

where h_+ is the plus polarization and $h_\times$ is the cross polarization. The GW energy density is then calculated with the following equation:

$$\Omega_{\mathrm{GW}}(f) = \frac{2}{T_{\mathrm{obs}}} \sum_0^N \frac{2\pi^2 f^3}{3H_0^2} \frac{dE}{df}, \tag{15}$$

where T_{obs} is the observation time and N is the number of sampled events. N is given by (9):

$$N(\alpha, \beta, z_{\mathrm{p}}, \mathcal{R}_0) = T_{\mathrm{obs}} \int_0^{z_{\mathrm{max}}} dz \frac{1}{1+z} \mathcal{R}(\alpha, \beta, z_{\mathrm{p}}, \mathcal{R}_0; z) \frac{dV_{\mathrm{c}}}{dz}. \tag{16}$$

After computing a theoretical value for N, the number of injections is determined with a Poisson process (see Appendix B).

In order to increase the observing time while keeping a reasonable run time, Ω_{GW} is averaged over n iterations. The number of injections in each is iteration still uses a Poisson process.

3.5. Combined Calculation of the SGWB

The combined method utilizes the same standard `bilby` prior dictionary and uses Equation 16 with a Poisson process to determine the number of samples.

The component masses are calculated from m_1 and q. Equation 12 can be used to find the chirp masses, which are then inserted into Equation 11. Equations 5, 11, and 13 are used to determine the final GW energy density spectrum. As in the Gridded Method, parameters f_{merge}, f_{ring}, f_{cutoff}, and σ are taken from (12).

4. RESULTS

The following section details the energy density spectra generated by each of the methods. The Gridded Method is used to explore the dependence of the SGWB on varying parameters in Sections 4.1.1 and 4.2. Monte Carlo sampling in both the Monte Carlo and Combined Methods causes the output energy density spectrum to differ between each run. Because the Gridded Method produces stable results, changes in the energy density spectrum are reliable.

4.1. Comparison of Methods

Figure 7 displays the spectra generated by all three methods. The blue curve shows the output from the Gridded Method, the red curve from the Monte Carlo Method, and the green curve from the Combined method. Ideally, all three curves are identical. However, the energy density for the Monte Carlo and Combined Methods are significantly greater than that for the Gridded Method. Each of the methods generates the same spectral shape for low frequencies, but they increasingly deviate frequencies above ≈ 100 Hz.
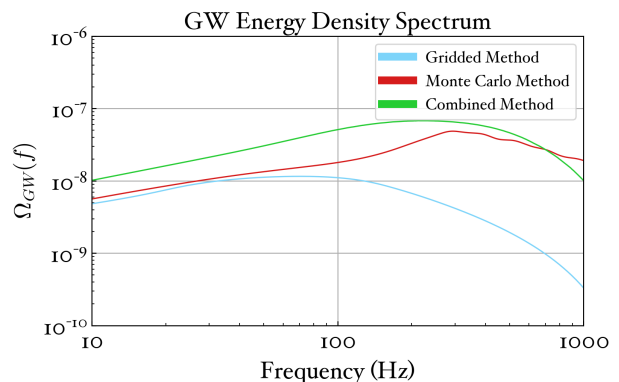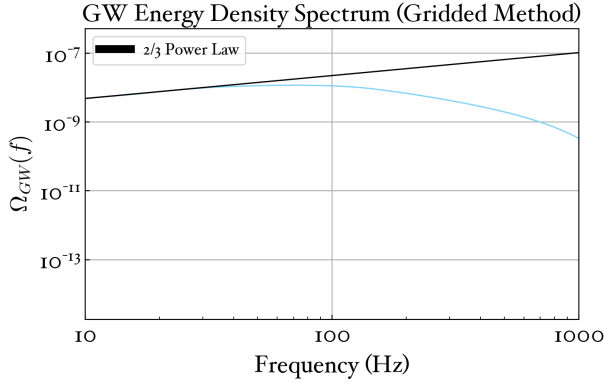

Figure 7. GW energy density spectra generated by the Gridded, Monte Carlo, and combined methods.

Figures 8, 9, and 10 individually show the energy density spectra for each method with an overlaid 2/3 power law. The Gridded and Combined Methods are generally consistent with the 2/3 power law at low frequencies, though the Combined Method has a slight deviation near 100 Hz. However, the Monte Carlo Method has significant discrepancies with the energy density curve more closely matching a 1/2 power law.

In addition, the Monte Carlo Method curve exhibits a peak at approximately 550 Hz, which is unexpected. There is also a slight peak near 130 Hz.

The Monte Carlo method also outputs inconsistent results, with the peak energy density ranging over an order of magnitude between runs. Due to memory space issues, only ≈ 20 events can be injected, resulting in non-smooth and inconsistent curves.
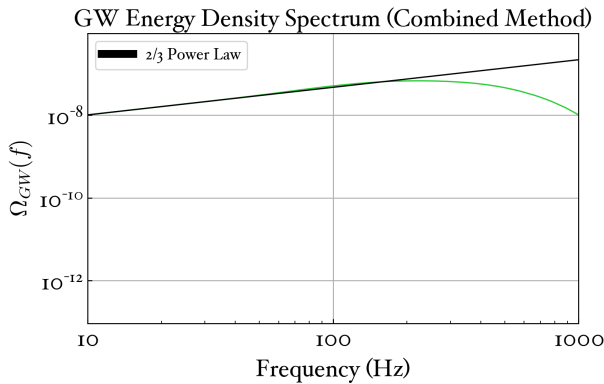
4.1.1. Effect of Maximum Black Hole Mass on the SGWB

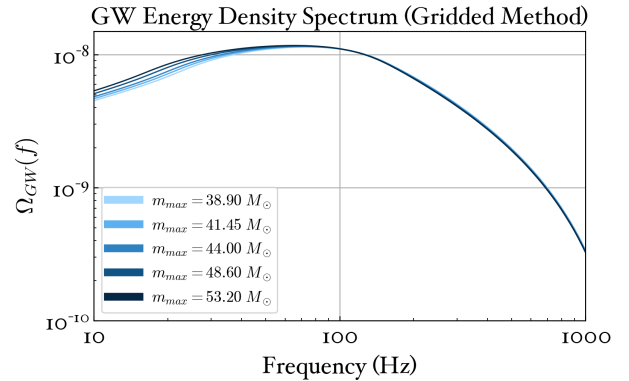**Figure 8.** GW energy density spectra generated by the Gridded Method with overlaid 2/3 power law.
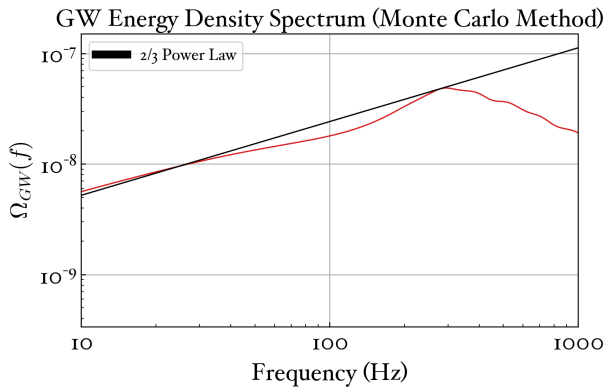
Figure 9. GW energy density spectra generated by the Monte Carlo Method with overlaid 2/3 power law.

Figure 10. GW energy density spectra generated by the Combined Method with overlaid 2/3 power law.

In order to investigate how the maximum black hole mass affects the SGWB, five different maximum masses are inserted into the Gridded Method. The chosen masses include the lower bound (38.90 $M_\odot$), average (44.00 $M_\odot$), and upper bound (53.20 $M_\odot$) given by (10). The remaining two masses, 41.45 $M_\odot$ and 53.20

$M_\odot$ average the two surrounding values to provide a representative spread of maximum masses.


Figure 11. GW energy density spectra generated by the Gridded method for varying maximum black hole masses.

Figure 11 demonstrates that increasing $m_{\max}$ is associated with a greater energy density and a lower-frequency peak, which is consistent with the well-documented relation that higher mass systems merge at lower frequencies.

4.2. *Effect of Merger Rate Parameters on the SGWB*

The effect of merger rate parameters on the SGWB is determined by varying each of the four merger rate parameters. Figure 13 depicts the merger rates that were inserted into the Gridded Method. The values for
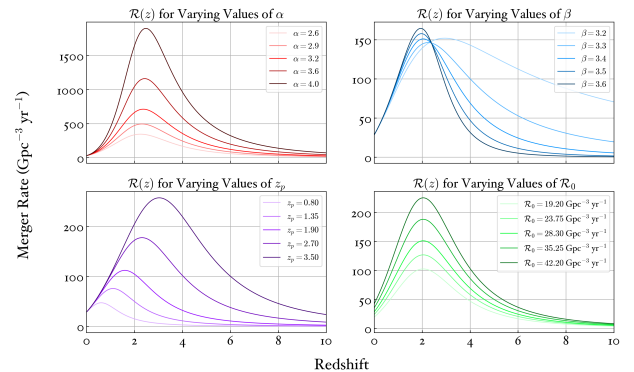
Figure 12. Merger rate generated for varying values of α, β, z_{p}, and $\mathcal{R}_0$ individually.

α and z_{p} are chosen from the bounds given by (9), while the values for $\mathcal{R}_0$ are based on (10). The values for β are chosen arbitrarily, as β immeasurable with current detectors.

The value of α affects the merger rate the most notably, especially as $\mathcal{R}(z)_{\mathrm{peak}}$ ranges from approximately

350 Gpc $^{-3}$ yr^{-1} to 1900 Gpc $^{-3}$ yr^{-1}. Larger values of α are associated with larger amplitudes and higher redshifts, and as α increases, there is a noticeable narrowing of the peak.

Increasing values of β shift the merger rate to higher amplitudes and redshifts. Large values of β also cause significant broadening of the curve at redshifts higher than z_{p}.

The value of z_{p} equally affects the merger rate in amplitude and redshift such that greater values of z_{p} correspond to higher amplitudes and lower redshifts.

The local merger rate $\mathcal{R}_0$ is directly proportional to the merger rate, meaning that $c\mathcal{R}_0$ will produce a merger rate of $c\mathcal{R}(z)$, where c is an arbitrary constant.
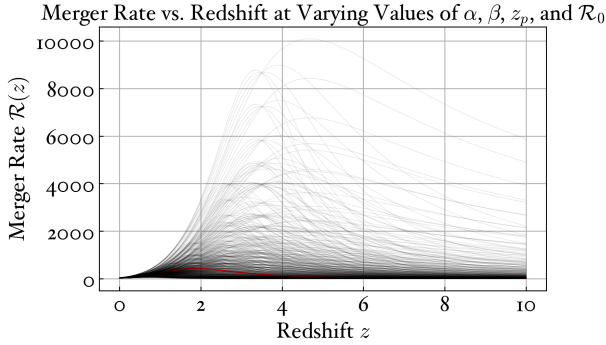

Figure 13. Graph displaying the merger rates generated by varying values of α, β, z_{p}, and $\mathcal{R}_0$, with the red curve representing the merger rate used across all methods.

Figure 13 displays the merger rates from 12 on a single graph. The observed variance is evidence for significant error in the merger rate.

The merger rates depicted in Figure 12 are inserted into the Gridded Method. The resulting spectra are shown in Figures 14, 15, 16, and 17.

α and $\mathcal{R}_0$ have the greatest impact on the energy density spectrum. Increasing values of α increase the amplitude of Ω_{GW} and shift the peak to lower frequencies, in contrast to the merger rate. $\mathcal{R}(z)$ linearly affects Ω_{GW}, as predicted.
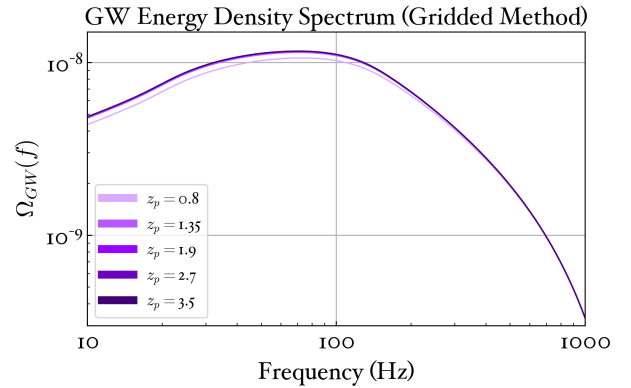
Changing the value of β and z_{p} does not significantly affect the SGWB amplitude or shape. One notable feature, though, is that increasing β and z_{p} dampens the effect on the SGWB.
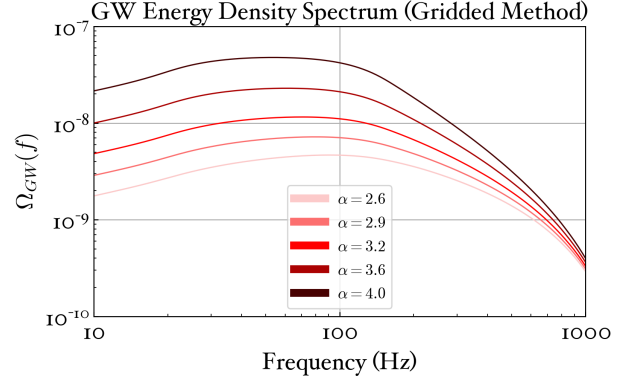
Figure 14. GW energy density spectra generated by the Gridded method for varying values of α.
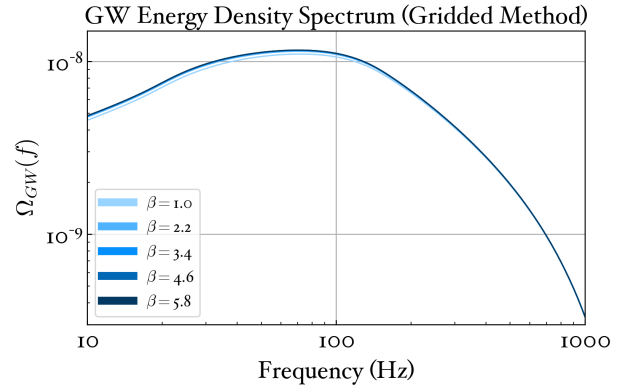
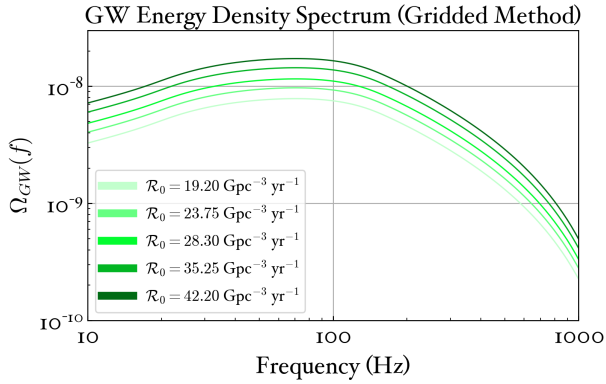**Figure 15.** GW energy density spectra generated by the Gridded method for varying values of β.

Figure 16. GW energy density spectra generated by the Gridded method for varying values of z_p.

Figure 17. GW energy density spectra generated by the Gridded method for varying values of $\mathcal{R}_0$.

REFERENCES

[1] Abbott, B. P., Abbott R., Abbott, T. D., et al. 2016, Phys. Rev. Lett., 116, 061102

[2] Piccinni, O. J. 2022, Galaxies, 10(3), 72

[3] Bustillo, J. C., Evans, C., Clark, J. A., et al. 2020, Commun. Phys., 3, 176

[4] Abbott, B. P., Abbott R., Abbott, T. D., et al. 2019, Astrophys. J., 886, 75

[5] Renzini, A. I., Goncharov, B., Jenkins, A. C., & Meyers, P. M. 2022, Galaxies, 10, 0

[6] Martynov, D. V., Hall, E. D., Abbott., B. P., et al. 2016, Phys. Rev., D 93, 112004

[7] Agazie, G., Anumarlapudi, A., Archibald, A. M., et al. 2023, ApJL, 951, L8

[8] Callister, T., Letizia, S., Shi, Q., et al. 2016, Phys. Rev., 6, 3

[9] Callister, T., Fishbach, M., Holz, D. E., & Farr, W. M. 2020, ApJL, 896, L32

[10] Abbott, R., Abbott, T. D., Acernese, F., et al. 2022, Phys. Rev. X, 13, 011048

[11] Callister, T. 2021, arXiv:2104.09508v1 [gr-qc]

[12] Ajith, P., Babak, S., Chen, Y., et al. 2008, Phys. Rev., D 79, 104017

[13] Khan, S., Chatziioannou, K., Hannam, M., et al. 2018, Phys. Rev., D 100, 024059

[14] Renzini, A. I., Romero-Rodriguez, A., Talbot, C., et al. 2023, AAS

[15] Aghanim, N., Akrami, Y., Ashdown, M., et al. 2020, A&A, 641, A6

APPENDIX

A. HUBBLE RATE

The Hubble parameter is a measure of the expansion of the universe in units of km s^{-1} Mpc^{-1}:

$$H(z) = H_0(\Omega_{\mathrm{R}}(1+z)^4 + \Omega_{\mathrm{M}}(1+z)^3 + \Omega_{\mathrm{k}}(1+z)^2 + \Omega_{\Lambda})^{1/2}, \tag{A1}$$

$$\Omega_{\mathrm{R}} = \Omega_{\gamma} + \Omega_{\nu} + \Omega_{\mathrm{GW}} + ..., \tag{A2}$$

where $H(z)$ is the Hubble parameter, H_0 is the current Hubble parameter ($z = 0$), z is redshift, and Ω is the energy density with R as the radiation component, M as the matter component, k as the curvature, and Λ as the cosmological constant, representative of dark energy. R is composed of photons, neutrinos, and GWs, while M is composed of baryons and cold dark matter. According to the Planck 2018 cosmological parameters, $H_0 = 67.66 \pm 0.42$ km s^{-1} Mpc^{-1}, $\Omega_{\mathrm{R}} = 9.182 \times 10^{-5}$, $\Omega_{\mathrm{M}} = 0.3111 \pm 0.0056$, $\Omega_{\mathrm{k}} = 0.001 \pm 0.002$, and $\Omega_{\Lambda} = 0.6889 \pm 0.0056$.[15]

The quantity Ω_{R} is particularly notable at high redshift, which is concurrent with the radiation-dominated era of the cosmological timeline, suggesting that Ω_{GW} becomes a measurable quantity when probing the early Universe.

B. POISSON PROCESS

A Poisson process is a method used for weighted sampling and is defined by the following equation:

$$p(n) = \frac{(\lambda t)^n}{n!} e^{-\lambda t}. \tag{B1}$$

In the context of the SGWB, p is the probability that n events occurs in an observing time t and λ is the total merger rate. Therefore, λt is equivalent to N in Equation 16. Equation B1 then represents a probability distribution from which to draw the number of injections.